ChemPubSoc Europe

DOI: 10.1002/cssc.201701291

CHEMSUSCHEM Full Papers

Reactive Electrophilic O^{I-} Species Evidenced in High-Performance Iridium Oxohydroxide Water Oxidation Electrocatalysts

Cyriac Massué,[a, b] Verena Pfeifer,[a, c] Maurice van Gastel,[d] Johannes Noack,[a] Gerardo Algara-Siller,[a] Sébastien Cap,*[a] and Robert Schlögl[a, b]

Although quasi-amorphous iridium oxohydroxides have been identified repeatedly as superior electrocatalysts for the oxygen evolution reaction (OER), an exact description of the performance-relevant species has remained a challenge. In this context, we report the characterization of hydrothermally prepared iridium(III/IV) oxohydroxides that exhibit exceptional OER performances. Holes in the O 2p states of the iridium(III/IV) oxohydroxides result in reactive O^{I-} species, which are identified by characteristic near-edge X-ray absorption fine structure (NEXAFS) features. A prototypical titration reaction with CO as a probe molecule shows that these O^{I-} species are highly susceptible to nucleophilic attack at room temperature. Similarly to the preactivated oxygen involved in the biological OER in photosystem II, the electrophilic O^{I-} species evidenced in the iridium(III/IV) oxohydroxides are suggested to be precursors to species involved in the O–O bond formation during the electrocatalytic OER. The CO titration also highlights a link between the OER performance and the surface/subsurface mobility of the O^{I-} species. Thus, the superior electrocatalytic properties of the iridium (III/IV) oxohydroxides are explained by their ability to accommodate preactivated electrophilic O^{I-} species that can migrate within the lattice.

Introduction

There is a growing consensus that, under acidic conditions, Ir-based oxygen evolution reaction (OER) catalysts are the most suitable candidates in terms of their activities and stabilities.[1] The current debate is focused on the understanding of the structure and chemical nature of such Ir structures to target the species with the highest intrinsic OER performance. To date, rutile-type IrO_2 has often been suggested to be the most suitable candidate owing to its stable OER activity under acidic conditions.[1b,2] However, there is growing evidence that quasi-amorphous or nanocrystalline Ir phases, which are more elusive to characterize, play a key role in acidic OER catalysis. Early electrochemical studies suggested that highly hydrated iridium oxide/hydroxides were formed during the oxidative activation of metallic iridium through electrochemical cycling[3] or reactive sputtering.[4] Vuković et al. noted that the mild thermal treatment of an anodically grown iridium oxide film (AIROF) at 200 °C improved the catalyst stability, whereas higher calcination temperatures led to the formation of crystalline IrO_2 and, consequently, a strong loss of OER activity.[3b] A similar evolution of the OER performance was reported recently by Reier et al., who observed superior OER performance for hydrous iridium oxide/hydroxides obtained through the calcination of iridium acetates at 250 °C.[5] Further calcination led again to the formation of IrO_2 and a sharp decrease in OER activity. Thus, the evolution of OER performance with the preparation conditions shows how crucial the nature of the prepared Ir phase is to the OER performance. The exact identification of the species responsible for the superior intrinsic activity of iridium oxide/hydroxide structures would allow the rational design of an optimized catalyst precursor; however, a large knowledge gap exists between molecular and crystalline Ir structures.

Recent efforts have been devoted to closing this gap.[6] The blue quasi-amorphous Ir phase often formed electrochemically was modeled for μ-oxo-bridged Ir^{IV} oligomers, which produced good agreement with the experimentally observed UV/Vis and Raman spectra.[6a] However, on the basis of EPR spectroscopy measurements of similar systems, Zhao et al. suggested that a

[a] Dr. C. Massué, Dr. V. Pfeifer, Dr. J. Noack, Dr. G. Algara-Siller, Dr. S. Cap, Prof. Dr. R. Schlögl
Department of Inorganic Chemistry
Fritz Haber Institute of the Max Planck Society
Berlin 14195 (Germany)
E-mail: sebastiencap@fhi-berlin.mpg.de

[b] Dr. C. Massué, Prof. Dr. R. Schlögl
Department of Heterogenous Reactions
Max Planck Institute for Chemical Energy Conversion
Mülheim an der Ruhr 45470 (Germany)

[c] Dr. V. Pfeifer
Helmholtz-Zentrum Berlin für Materialien und Energie GmbH
Elektronenspeicherring BESSY II
Berlin 12489 (Germany)

[d] Dr. M. van Gastel
Department of Molecular Theory and Spectroscopy
Max Planck Institute for Chemical Energy Conversion
Mülheim an der Ruhr 45470 (Germany)

Supporting Information and the ORCID identification number(s) for the author(s) of this article can be found under https://doi.org/10.1002/cssc.201701291.

significant part of the OER-active Ir compound was in the Ir^{III} state.[7] The relevance of mixed oxidation states in iridium oxide/hydroxides in the OER was further highlighted by Minguzzi et al., who performed in situ X-ray absorption spectroscopy (XAS) on Ir films during the OER.[8]

These results reveal that the description of the electronic structure of iridium oxide/hydroxides is crucial for understanding their superior OER performances. X-ray photoemission spectroscopy (XPS) has been used in some studies, and the Ir oxidation states were assigned on the basis of the binding-energy (BE) shifts.[9] However, it is essential to point out that the analysis of the XPS and XAS spectra of oxidic Ir compounds is by no means trivial, as the structure of the electron–hole pair excitation spectra has to be taken into account for the consideration of the core levels. To address the ongoing debate on Ir speciation, Pfeifer et al. recently developed a reliable model of the electronic structure of iridium oxides. This model showed that the Ir4f peak obtained in the XPS spectrum for rutile-type IrO_2 cannot be fitted with the standard Doniach–Šunjic line shape that is usually applicable to metallic conductors.[10] This model was adapted for a quasi-amorphous iridium oxohydroxide benchmark, and the presence of an additional species, namely Ir^{III}, was revealed. Counterintuitively, the Ir^{III} component shows up at higher binding energies than the Ir^{IV} component; therefore, the Ir speciation for iridium oxides should not be assigned solely from the binding-energy shifts. The authors also assigned a characteristic pre-edge feature in the near-edge X-ray absorption fine structure (NEXAFS) spectrum of the O K-edge of iridium(III/IV) oxohydroxide to O2p hole states, which result in formally O^{I-} species that emerge in conjunction with Ir^{III} species. Interestingly, such potentially highly electrophilic O species have been debated in the context of the biological OER in Photosystem II, in which the formation of such preactivated O sites would enable nucleophilic attack and subsequent O–O bond formation.[11] Pfeifer et al. suggested that the ability of iridium(III/IV) oxohydroxides to accommodate reactive electrophilic O^{I-} species could explain their superior electrocatalytic performances through a similar mechanism.[12]

To test this hypothesis and study the functional relationship between the electronic structure of iridium(III/IV) oxohydroxides and their OER performances, we prepared a family of iridium oxohydroxides through an innovative microwave-supported (MW-supported) hydrothermal synthesis.[13] The base/Ir ratio in the initial precursor solution was identified as a key parameter to tune the structural properties and OER performance. The systematic variation of this parameter yielded a family of iridium oxohydroxides and provided an opportunity to uncover correlations between the structural features and OER performance to establish functional links.[13] A moderate excess of base led to highly nanostructured, nanocrystalline, Ir^{III}-rich oxohydroxides with outstanding OER performances. Higher amounts of base led to the formation of core–shell structures with metallic Ir cores embedded deeply into an oxidic Ir shell approaching the IrO_2 stoichiometry. Such compounds featured higher K contents, which could be linked to changes in the nanocrystalline structure of the iridium oxohydroxides, and resulted in lower OER performances.

In the present study, we have aimed to relate the electronic structures of the iridium oxohydroxides to their electrocatalytic performances in the OER. For this purpose, the MW-prepared iridium oxohydroxides were analyzed through a series of complementary characterization techniques to obtain a thorough description of the present compounds. First, a careful TEM investigation and the interpretation of the Raman spectra through DFT-calculated models were used to establish the distinction of the materials from microcrystalline IrO_2. Furthermore, the theoretical model of the electronic structure of iridium oxides established by Pfeifer et al.[10] was used to analyze the synchrotron-based X-ray photoemission and absorption spectra of the iridium oxohydroxides. The XPS spectra were analyzed to determine which Ir species were present. NEXAFS was used to identify reactive oxygen species such as the formal O^{I-} species reported by Pfeifer et al. for a similar compound.[10] To quantify the amount and electrophilicity of such reactive O species, we used reactive CO titrations, as proposed by Wang et al.[10b,14] Quantitative trends were compared to OER performance indicators to identify OER-relevant features. The identification of such features paves the way towards the targeted design of synthesis strategies for efficient Ir-based OER-electrocatalyst precursors for industrially relevant applications.

Results and Discussion

In the following paragraphs, we compare the structural and chemical variations within the family of MW-produced compounds and the corresponding evolution of the OER performance to establish functional links. For rapid identification, the samples prepared through the MW-supported hydrothermal synthesis strategy are identified as "MW_*X*", and *X* identifies the varied synthesis parameter, that is, the base/iridium ratio (KOH/Ir = *X*:1; see the Supporting Information, Table S1).

OER performance

The classical indicators of OER activity and stability (summarized in Figure 1) were used to compare the electrocatalytic performances of the MW-produced iridium oxohydroxides and

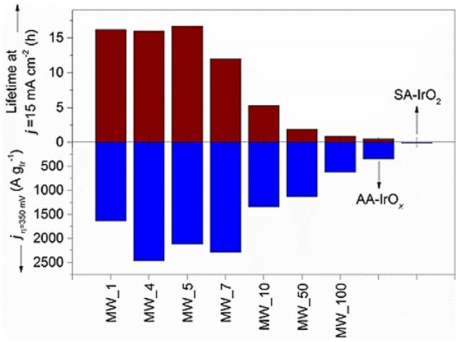

Figure 1. The OER activity reflected by the current density *j* at 350 mV overpotential (blue bars) and OER stability indicated by stable operation at 15 mA cm^{-2} (red bars) tend to worsen for the MW samples as the base/Ir ratio increases. The performances are compared with those of two commercial benchmarks (right).

Ir benchmarks. Within the MW-produced sample batch, the OER performance was best for a low initial KOH/Ir ratio, which resulted in a combination of high current densities (*j*) at 350 mV and long lifetimes in the chronopotentiometric (CP) tests.

The samples prepared with KOH/Ir = 4:1 and 5:1 exhibited the best OER performances, and an optimal synthesis yield was obtained for KOH/Ir = 5:1.[13] In contrast, at KOH/Ir ≥ 7:1, the performance decreased rapidly. Through H_2 temperature-programmed reduction (TPR), we showed that the average oxidation state increases gradually from +3.2 for KOH/Ir = 1:1 to +3.8 for KOH/Ir = 50:1. However, despite its similar structural features (average oxidation state, TPR profile, chemisorbed water fingerprint), the iridium oxohydroxide benchmark AA-IrO_x showed the worst performance by far of the nanocrystalline iridium oxohydroxide compounds, and this provided us with an incentive to search for distinctive features beyond the mixed Ir oxidation state in our MW-produced iridium oxohydroxides.

TEM investigation of beam-sensitive iridium oxohydroxide

In our previous report on the MW-supported hydrothermal synthesis of iridium oxohydroxides, we mentioned the great difficulty of studying such compounds through electron microscopy owing to the rapid transformation of the nanocrystalline oxidic Ir phase into metallic iridium.[13] As a strategy to avoid radiation damage, we chose to encapsulate the MW-produced iridium oxohydroxide between graphene sheets.[15] We chose the best catalyst, MW_5, which is also the purest compound produced in terms of contamination with Cl and metallic Ir traces.[13] However, no significant improvement against radiation damage was observed during the high-resolution transmission electron microscopy (HRTEM) imaging with electron dose rates greater than $10^5\ e\,nm^{-2}\,s^{-1}$. Nevertheless, details of the intrinsic structure of MW_5 were obtained through the electron diffraction (ED) technique. Through the comparison of an ED pattern with an electron dose rate of $80\ e\,nm^{-2}\,s^{-1}$ (Figure 2a) and an ED pattern with a high electron dose rate (Figure 2b) of $10^5\ e\,nm^{-2}\,s^{-1}$, it was possible to observe the structural transformation caused to the sample by electron irradiation. The diffraction patterns were analyzed with the profile-analysis tool PASAD.[16]

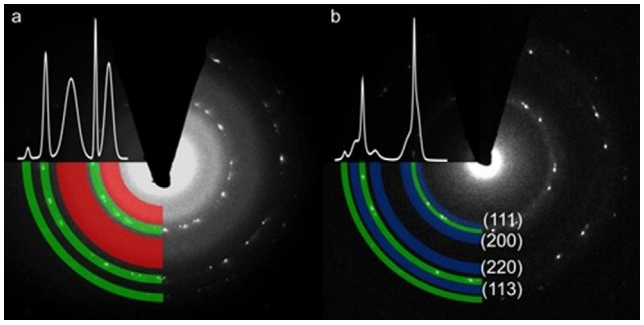

Figure 2. The selected-area electron diffraction (SAED) patterns and radial profiles for MW 5 (a) under low electron dose and (b) with high electron dose show the complete transformation of the initial iridium oxohydroxide to metallic iridium after beam irradiation.

The corresponding radial profiles and diffraction patterns are shown in Figure 2. The contributions shown in green correspond to the *d* = 2.13, 1.23, and 1.07 Å graphene spacings. The analysis of the recorded ED pattern exposed to an intense electron beam (Figure 2b) reveals intensity rings (blue arcs) that are attributed to the *d*-spacings of the (111), (200), (220), and (113) planes of cubic metallic iridium (see ICSD 87-715); therefore, most of the iridium was reduced under the influence of the high dose beam. On the other hand, the radial profile obtained from the low-dose ED pattern (Figure 2a) exhibits a very distinct shape with two broad contributions at spacings corresponding to *d* = 2.69 and 1.63 Å (red arcs). The *d*-spacings observed initially for MW_5 confirm that the distribution of elements inside the nanocrystalline iridium oxohydroxide is very distinct from that in crystalline IrO_2. The reflections for IrO_2 would be expected at *d* = 3.18, 2.58, 1.70, and 1.59 Å, which correspond to the (110), (101), (211), and (220) planes, respectively, of IrO_2. This in line with the discrepancy between the Ir/O ratio of 1:2 expected for IrO_2 and the bulk Ir/O stoichiometry determined through H_2-TPR for the iridium oxohydroxides. These results confirm that the nanocrystalline iridium oxohydroxides are not simply small highly distorted IrO_2 crystallites and instead constitute a distinct phase.

Raman spectroscopy of iridium oxohydroxides

To identify the key structural features of the quasi-amorphous OER-active Ir compounds, Raman spectroscopy was used recently by Hintermair et al.[6a,b] The authors attributed signals at $\tilde{\nu} = 560$ and $730\ cm^{-1}$ to the vibrational Raman-active modes of a planar bis-μ-oxo Ir^{IV} dimer formed under OER potential. The observed modes were distinct from the well-known contributions of rutile IrO_2.[17] The present batch of iridium oxohydroxides provide an opportunity to relate changes in the recorded Raman spectra to structural variations between the samples.

The Raman spectra for five MW-prepared samples are shown in Figure 3. A qualitative five-component Gaussian fit was performed (see Figure S2) and resulted in two weak contributions at $\tilde{\nu} = 320$–340 (I) and 675–$720\ cm^{-1}$ (V). Three major contributions were identified at $\tilde{\nu} = 420$–465 (II), 510–520 (III), and 565–$600\ cm^{-1}$ (IV). The fitting parameters show that the modes identified by component III clearly gain in importance for increasing KOH/Ir ratios; these modes represent 22% of the integrated signal for MW_4 compared with 64% for MW_100.

To interpret the observed spectra, we established a theoretical model based on the experimental evidence. Considering that the average oxidation state determined through H_2-TPR for the oxidic phase approaches Ir^{IV} with increasing KOH/Ir ratio and that the compounds are highly hydrated,[13] we chose hydrous Ir^{IV} oligomers as a starting point to find a model structure for the synthesized compounds. Owing to the suspected oligomeric nature of our compounds, we chose bis-μ-oxo units to link the Ir atoms, in accordance with the structure suggested by Hintermair et al.[6a,b] The optimized structure obtained

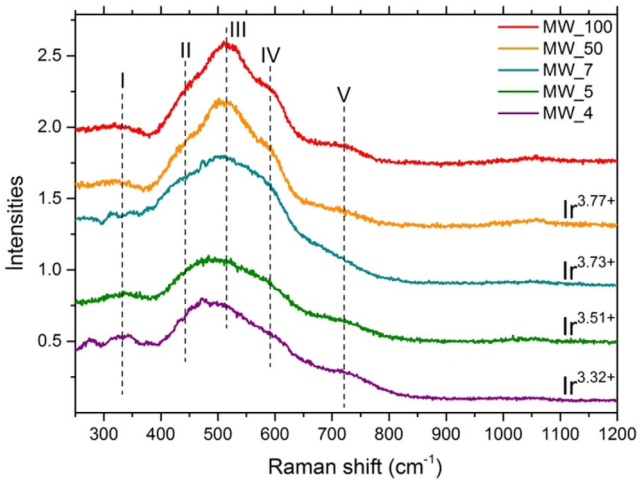

Figure 3. The Raman spectra of the MW-prepared iridium oxohydroxides show distinctive features in the $\tilde{\nu}=300$–$750\ cm^{-1}$ range. The average bulk oxidation states indicated on the right were quantified through H_2-TPR.

through DFT for a formally Ir^{IV} trimer involving μ-oxo bridges, coordinated water molecules, and hydroxy terminations is shown in Figure 4. The calculated Raman spectrum shows that contributions I and V correspond to vibrations localized mostly on the hydroxy groups and surrounding water molecules, albeit with calculated frequencies that are systematically too high, as expected for a small trimeric unit. On the other hand, the calculated Raman modes between $\tilde{\nu}=480$ and $645\ cm^{-1}$ involve the bridging μ-oxo groups, which produce a series of concerted asymmetrical stretching, rocking, and bending modes.

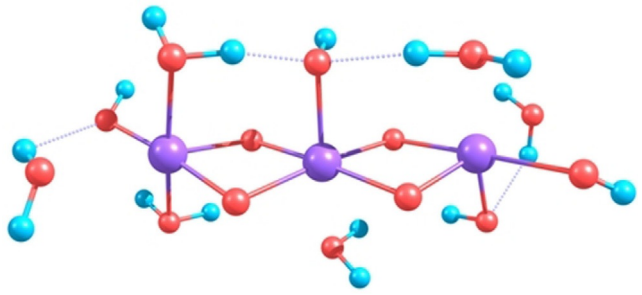

Figure 4. DFT-calculated structure of a bis-μ-oxo Ir^{IV} trimer. Blue H, red O, and purple Ir.

To model the presence of Ir^{III} species in the iridium oxohydroxides, the calculated trimeric Ir^{IV} structure was reduced to a formally Ir^{IV}–Ir^{III}–Ir^{IV} trimer. The DFT-based optimization of the structure results in a rearrangement of the protons such that two of the μ-oxo-bridging species become bridging hydroxy groups (Figure 5).

The resulting calculated Raman-active modes do not include concerted motions, such as the rocking of all four bridging oxygen atoms, as predicted at $\tilde{\nu}=553\ cm^{-1}$ for the Ir^{IV} trimer. In general, the incorporation of Ir^{III} species diminishes the number of concerted Raman-active vibrations of the bridging

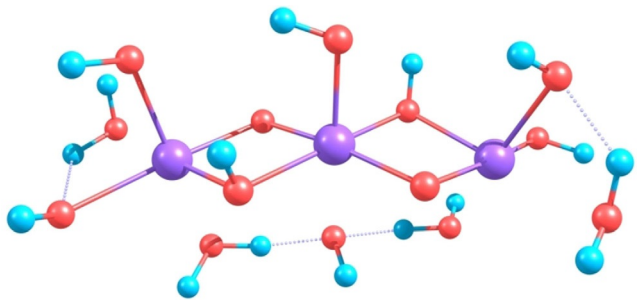

Figure 5. DFT-calculated structure of a reduced $Ir^{III/IV}$ trimer. Blue H, red O, and purple Ir.

oxygen species, and this could explain the lower intensity of the modes contributing to component III. The spectrum is dominated by μ-oxo vibrations. These vibrations are more localized than those of the oxidized trimer and, therefore, shifted to higher frequencies. The dominant Raman-active modes are shown in Figures S3 and S4. The spontaneous protonation of two oxo bridges upon the reduction of the trimeric cluster in silico indicates that Ir^{III} species may disrupt the bis(μ-O^{2-}) bridging motif, and this in turn may lead to an increased amorphicity and a concomitant decrease in the intensity of the oxo-related modes in the Raman spectrum (see Figure S5). Thus, our simple DFT-based model provides a first interpretation of the complex Raman contributions of iridium oxohydroxides and highlights the importance of bis(μ-O^{2-}) bridging motifs.

X-ray photoemission spectroscopy

In our report on the synthesis of the present batch of pure iridium oxohydroxides, we highlighted the low-temperature reduction features of the compounds and suggested a mixed $Ir^{III/IV}$ oxidation state.[13] The observed trends in the average oxidation state seemed to indicate that the OER performance improved for lower Ir^{IV}/Ir^{III} ratios (Figure 1).

To confirm the $Ir^{III/IV}$ nature near the surfaces of the compounds, XPS measurements were performed for MW_5, MW_10, MW_50, and MW_100. First, the electron densities measured at the Fermi edge for all samples are in line with those observed by Reier et al.[5b] and confirm the quasimetallic conductivity of the iridium oxohydroxide phase (see Figure S6). Furthermore, the analysis of the Ir 4f line shape confirms that the samples are in a mixed $Ir^{III/IV}$ state, and there is a general trend towards higher Ir^{IV}/Ir^{III} ratios for higher KOH/Ir ratios (Figure 6). The presence of metallic Ir in the surface region can be excluded, as no contributions were detected at BE = 60.9 eV (Figures 6 and S7).[10a,18] This is in line with the core–shell structure with a metallic Ir^0 core embedded in a thick oxidic overlayer observed through SEM energy-dispersive X-ray spectroscopy (SEM-EDX) for higher KOH/Ir ratios.[13] According to the fit model described in the introduction,[10] Ir^{III} species contribute with an Ir $4f_{7/2}$ binding energy of 62.4 eV, whereas Ir^{IV} species are found at a lower binding energy of 61.8 eV. The Ir 4f peaks recorded at photoelectron kinetic energies of 130 and 450 eV and fitted to this model show a similar picture (see Figure S7),

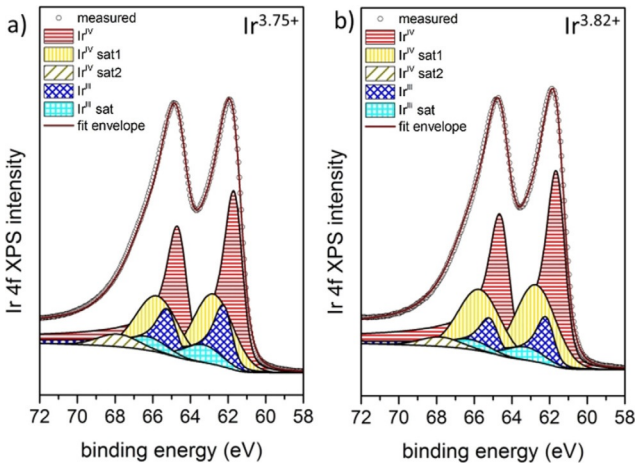

Figure 6. The XPS spectra of (a) MW_5 and (b) MW_100 in the Ir 4f region for 450 eV kinetic energy show the contributions from Ir^{III} and Ir^{IV} species. The average oxidation state calculated from the fit is indicated in the top-right corner.

which indicates that Ir^{III} species are present not only at the surface but also deeper inside the bulk. This finding is also in line with the large fraction of Ir^{III} species suggested by the average oxidation state determined through H_2-TPR (Figure 1) and suggests a homogenous distribution of Ir^{III} and Ir^{IV} species throughout the oxidic Ir phase. The concomitant decrease in OER performance and Ir^{III}/Ir^{IV} ratio observed with increasing KOH/Ir ratio indicates the relevance of Ir^{III} species to the OER performance. It is important to highlight our finding of a possible link between Ir^{III} species and OER performance. The unambiguous description of the electronic structure of active Ir-based OER catalysts has remained a challenge so far, although a few studies have highlighted the possible role of mixed Ir oxidation states.[8b, 10a]

X-ray absorption spectroscopy

Recent studies, such as that conducted by Fierro et al.,[19] have highlighted that part of the oxygen evolved during the Ir-catalyzed OER originates from the iridium oxide itself. Consequently, oxygen species from the Ir lattice are involved in the catalytic process. Hence, in addition to an understanding of the active metal centers, the description of the O species present in the surface region is of prime importance to understanding the OER reactivity. For this purpose, Reier et al. analyzed the O 1s spectra of their mixed Ni/Ir electrocatalysts before and after the reaction and found a possible link between OER reactivity and the coverage with reactive surface hydroxy groups.[20] We generally observed a higher XPS intensity at BE ≈ 531.1 eV for the more active samples (see Figure S7), and this peak compares to the contribution at BE = 531.4 eV attributed by Reier et al. to reactive surface hydroxy groups. However an unambiguous deconvolution of the O 1s peak is rendered difficult by the manifold contributions to the O 1s spectra from water, hydroxy groups, lattice oxygen atoms, and other possible O-containing functional groups. Therefore, we decided to probe the density of the unoccupied O 2p states through the NEXAFS analysis of the O K-edge. Pfeifer et al. used this technique to observe characteristic features in the O K-edge of commercially available iridium oxohydroxides. On the basis of theoretical calculations, they could assign these features to electronic defects in the anionic framework.[10]

To test whether such electronic defects are also present in our MW-produced iridium oxohydroxides, we measured the O K-edges of samples MW_5, MW_10, MW_50, and MW_100. The NEXAFS spectra of the MW-produced iridium oxohydroxides are show in Figure 7 together with those of the reference samples $AA\text{-}IrO_x$ and $SA\text{-}IrO_2$ for comparison. The main resonances of the rutile-type reference sample $SA\text{-}IrO_2$ are found at excitation energies of 530 and 533 eV. The pre-edge feature observed for $AA\text{-}IrO_x$ at 529 eV was attributed previously to O 2p hole states additionally present in the iridium oxohydroxide reference sample.[10] The authors suspected that these electrophilic O^{I-} species played a key role in the OER reactivity, as the $AA\text{-}IrO_x$ containing such species is vastly superior in terms of OER performance compared with O^{I-}-free $SA\text{-}IrO_2$. Furthermore, the model established a direct link between the presence of such O^{I-} species and Ir^{III}.[10a]

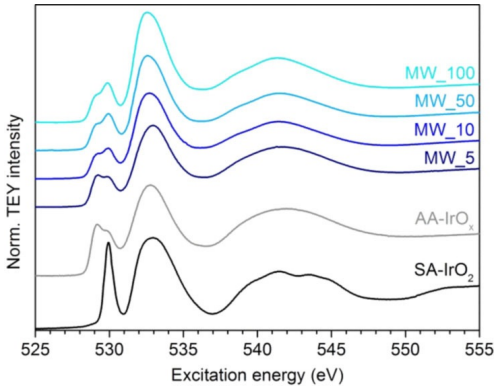

Figure 7. NEXAFS spectra for the MW-prepared iridium(III/IV) oxohydroxides and the reference samples $SA\text{-}IrO_2$ and $AA\text{-}IrO_x$.

A comparison of the O K-edge spectra of the MW-produced iridium oxohydroxides from the present study shows that the ratio of the features at 529 and 530 eV changes continuously with increasing KOH/Ir ratio; MW_5 exhibits the strongest peak at 529 eV and, thus, the highest amount of suspected formally O^{I-} species. As MW_5 also shows the best OER performance, we suggest a direct link between a higher amount of Ir^{III}-stabilized O^{I-} species and improved OER performance for our batch of MW-produced iridium oxohydroxides. The suspected OER reactivity of these peculiar O species and the fact that their chemical environment seems to stabilize them in the ex situ catalyst takes us a step closer to an understanding of why the MW-produced iridium(III/IV) oxohydroxides are such excellent precursors for OER electrocatalysis. Nonetheless, $AA\text{-}IrO_x$ also exhibits a strong feature at an excitation energy of 529 eV despite its much weaker OER performance than those of our MW-produced iridium oxohydroxides. This observation implies that the trend observed within the MW sample batch cannot

be taken as an absolute indicator of OER performance and that other factors must play a key role. These findings were an incentive to investigate the chemistry of the observed O^{I-} species through a reactive probe technique.

CO titration of reactive oxygen species

The low-temperature oxidation of CO is used commonly as a prototypical reaction for the study of heterogeneous catalyst systems.[10b,21] Typical systems consist of noble-metal nanoparticles such as Pd,[21] Pt,[22] or Ir[23] supported on partially reducible oxides. The noble metal is usually described as a preferential adsorption site for CO, whereas the oxide support is thought to gather activated O_2 from the feed for the oxidation of CO to CO_2. In the absence of O_2 in the feed, reactive oxygen pools hosted by the catalyst lattice can react with CO. Recently, Lin et al. described the preferential oxidation of CO (PROX) by an Ir/Fe(OH)$_x$ system.[23] They showed that CO reacted with OH species adsorbed on the Fe support with much lower activation energies than that for the reaction with adsorbed O_2, and complete CO oxidation was observed at room temperature (RT). In a similar approach, Wang et al. used such CO titrations at RT to quantify reactive oxygen species (designated as O*) in Co_3O_4 catalysts, which were identified as O_2^- and O^- anions through O_2-TPD.[14] In the context of a stoichiometric reaction, CO is used as a probe molecule to titrate O*. Inspired by these results, we decided to assess the reactivity of the observed O^{I-} species through such a CO-titration approach at RT. To obtain a quantitative insight into the amount of available O*, including the suspected O^{I-} species, the Ir samples were exposed to a 1% CO/He flow at RT. The detected CO_2 is assigned to the stoichiometric reaction of CO with the O* present in the Ir compounds [Eq. (1)].

$$IrO_x{-}O^{(n-)}* + CO \rightarrow IrO_x + CO_2 + n\,e^- \quad (1)$$

The AA-IrO$_x$ reference compound, which consists of a similar iridium (III/IV) oxohydroxide material,[10] also produced CO_2 under the same conditions. Only the crystalline SA-IrO$_2$ showed no CO_2 evolution during the CO titration (Figure S9). We conclude that CO oxidation at RT in an inert carrier gas is specific to iridium (III/IV) oxohydroxide compounds and enables the titration of O* present in these compounds.

To verify whether the O* pool could be replenished, in a separate experiment, MW_5 was subjected to a water-saturated He stream for 1 h at RT after the first CO titration. During a subsequent switch to 1% CO/He, no sign of a second CO_2 emission could be detected. This shows that the O* source could not be regenerated from H_2O at RT, unlike the reactive hydroxy groups evidenced by Li et al. for PROX with the Ir/Fe(OH)$_x$ system.[23] In a similar experiment, we also showed that the O* could not be replenished in a 1% O_2/He stream at RT. These results indicate that the O* species evidenced in iridium oxohydroxides are not reactive hydroxy groups or preadsorbed activated O_2.

To identify the nature of the O* species, in a parallel study, Pfeifer et al. performed a synchrotron-based quasi in situ study of the CO-titration procedure with AA-IrO$_x$.[12] The AA-IrO$_x$ benchmark was exposed to CO in a near-ambient-pressure XPS (NAP-XPS) reactor.

As for the RT experiment discussed above, CO_2 evolution was detected for dosing with pure CO. No changes to the Ir 4f XPS signal could be detected. However, a clear loss in the NEXAFS pre-edge resonance of the O^{I-} species at 529 eV indicated that these are the species that were consumed during the oxidation of CO to CO_2 at RT. From this, we conclude that the O* species titrated in the RT CO experiment are identical to some of the O^{I-} species evidenced in the NEXAFS analysis of the O K-edge. Owing to the similar nature of AA-IrO$_x$[10a] and our MW-produced iridium oxohydroxide, we propose that the electrophilic reactivity of O^{I-} species with CO at RT is a general feature of iridium oxohydroxides [Eq. (2)].

$$IrO_x{-}O^{I-} + CO \rightarrow IrO_x + CO_2 + e^- \quad (2)$$

Despite their similar electronic structures (Figure 7), AA-IrO$_x$ and the MW-produced compounds exhibited very different OER performances. In this regard, the analysis of the CO_2-evolution curves shows that the samples can be distinguished by the availability and reactivity of the titrated O^{I-} species. First, the quantification of the total amount of CO_2 evolved for each sample (Figure 8b) shows that up to 0.32 CO_2 molecules are evolved per Ir site for MW_5. If only surface O^{I-} species were titrated, this would amount to a surface concentration of one O^{I-} species per 13 Å^2, as calculated from the specific surface area of MW_5. Such a high surface concentration of O^{I-} species is unlikely and suggests that the titration of O^{I-} is not limited to the surface and involves O^{I-} located deeper in the bulk. Such a hypothesis is in line with the sluggish CO_2 evolution, which proceeds for hours for the compounds richest in O^{I-} ($1{:}1 \leq KOH/Ir \leq 10{:}1$). The involvement of subsurface O^{I-} species indicates that the O^{I-} species can migrate to the surfaces of the iridium oxohydroxides during the CO titration at RT. A sharp decrease in the total evolved CO_2 is observed for samples MW_50 and MW_100 as well as AA-IrO$_x$; therefore, fewer O^{I-} species were accessible to CO for these three sample (Figure 8b). A decreasing amount of available O^{I-} with increasing KOH/Ir ratio is in line with the diminution of the NEXAFS resonance at 529 eV (Figure 7). However, the NEXAFS spectrum of AA-IrO$_x$ also showed a higher O^{I-}/O^{II-} ratio than that of MW_5. This is in contrast with the relatively low amount of titrated O^{I-} species. Therefore, although a relatively high amount of O^{I-} species was detected through the subsurface-sensitive NEXAFS technique, only a relatively low amount of these species was available for reaction with CO. We conclude that the observed trends in evolved CO_2 also reflect to an important extent the ability of subsurface O^{I-} species to migrate to the sample surface to react with CO. For AA-IrO$_x$, this mobility is less pronounced than that for the MW-produced samples. The factors controlling O^{I-} mobility are still be identified.

To study the OER relevance of the titrated electrophilic O^{I-} species, the Ir-specific OER mass activities of the iridium oxohydroxides were compared to the amounts of titrated O^{I-} species. As shown in Figure 8c, a loose linear correlation was ob-

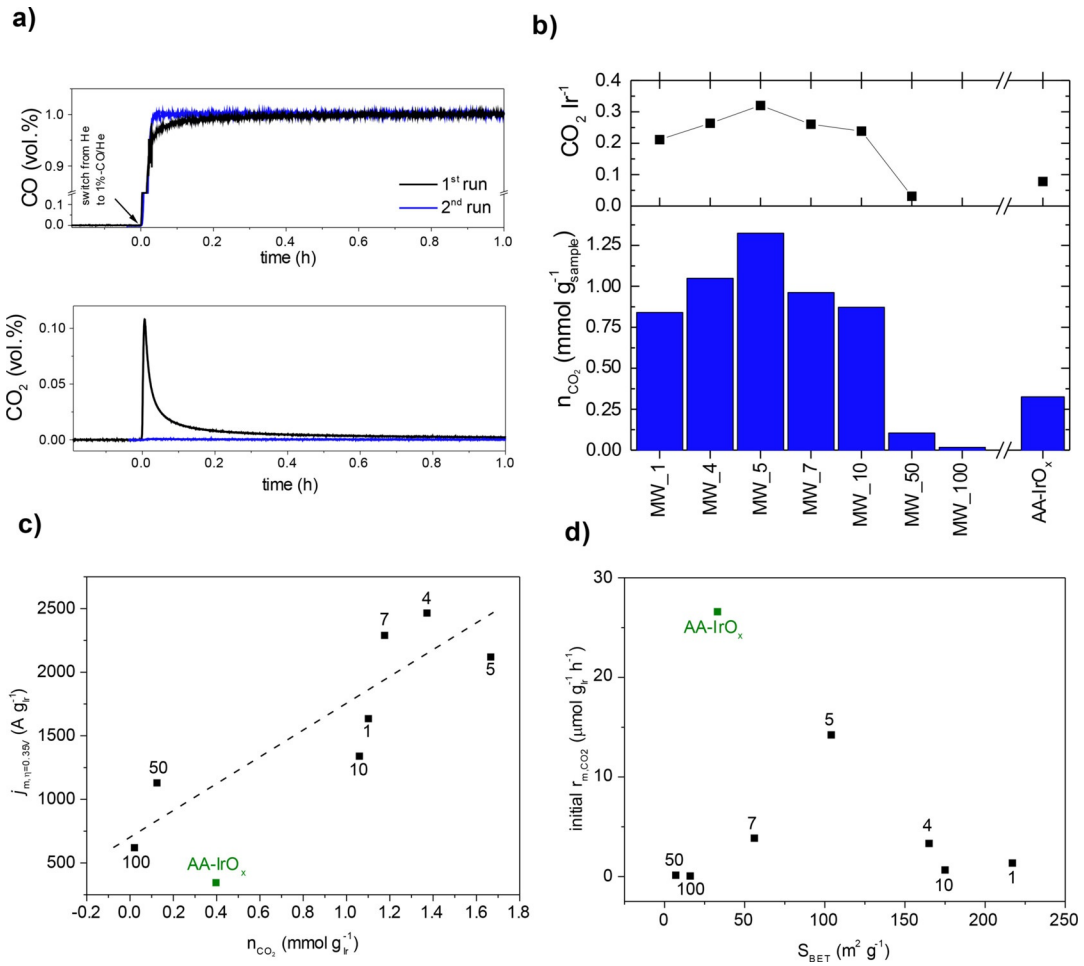

Figure 8. (a) The gas-stream composition for the test of one of our best OER catalysts, MW_5. During the initial switch from 100% He to 1% CO/He (100 mL min^{-1}), a clear transient CO_2 signal was observed, and this indicates that CO was oxidized by a finite oxygen source originating from the iridium oxohydroxide. Once no more CO_2 evolution was detected, the reactor was purged with He, and the sample was again subjected to a 1% CO/He stream. During this second titration, no CO_2 evolution was detected (blue CO_2 signal, Figure 8 a), and this result confirms the stoichiometric nature of the reaction. The procedure was repeated for every compound (see Figure S9). For each sample, we confirmed the irreversible nature of the reaction observed as transient CO_2 evolution during the initial switch to 1% CO/He.

served between the amount of titrated O^{I-} species and the OER activity for the MW compounds. Therefore, the best OER catalysts also apparently contained the highest amount of O^{I-} species, whereas the samples with weaker OER performances (higher KOH/Ir ratios) evolved only little CO_2, that is, they exhibited fewer available O^{I-} species. We conclude that the titrated O^{I-} species are involved directly in the superior OER performance of the MW-produced iridium oxohydroxides. This suggests that the amount of available electrophilic O^{I-} species detected through CO titration could act as an indicator of the OER performance of the MW-produced iridium oxohydroxides.

However, the comparison of the MW-produced samples and the AA-IrO_x benchmark suggests that the OER performance involves a more complex set of parameters. The AA-IrO_x sample evolved a significantly higher amount of CO_2 than the MW_50 and MW_100 samples, which suggests that it contains more accessible O*. Nonetheless, it is by far the iridium oxohydroxide with the worst OER performance (Figure 1), which places it outside the trend observed for the MW-produced compounds (Figure 8 c). This shows that isolated descriptors such as the amount of accessible O^{I-} species should only be used for a batch of samples prepared under the same conditions, such as the MW-prepared iridium oxohydroxides.

A closer look at the CO_2-evolution curves (Figure S9) shows that the CO_2 evolution for AA-IrO_x was initially very fast but levelled off rapidly after 1 h, whereas the MW-produced iridium oxohydroxides evolved CO_2 for several hours. This indicates different O^{I-} reactivities between the iridium oxohydroxides and the AA-IrO_x benchmark. In this regard, the initial CO_2 evolution rate can be seen as a useful descriptor as it yields information about the reactivity of the first O^{I-} species to react with CO, which are probably mostly located at the surface. The initial Ir-mass-specific CO_2 evolution rate for the MW compounds as a function of the specific surface area (S_{BET}) is shown in Figure 8 d. If it is assumed that the initial rate reflects only the titration of surface species, one would expect a linear increase with S_{BET}. Instead, the result is a volcano-type plot, which shows the prominent nature of MW_5 as it exhibits the highest initial CO_2 evolution rate of the MW compounds. On the other hand, MW_4 exhibits a significantly lower initial rate

despite its similar OER performance. This suggests that the OER performance does not depend solely on the reactivity of surface O^{I-} species.

The observed differences in the initial evolution rates and the total amount of evolved CO_2 lead us to suggest the following scenario: The surface O^{I-} species present in AA-IrO_x exhibit a higher electrophilic reactivity towards CO than those in the MW compounds. However, the rapid arrival of evolved CO_2 in the plateau region (Figure S9) suggests that, once the surface O^{I-} species have been consumed, the O^{I-} species located deeper in the bulk do not participate in the reaction to the same extent as those in the MW compounds.

These observations indicate clearly that a complex set of parameters govern the O^{I-} titration mechanism. The ability of O^{I-} species located in the bulk to migrate to the surface seems to play a key role. Thus, the environment of the O^{I-} species, namely, the hydroxy groups such as those highlighted by Reier et al. as possible descriptors of OER reactivity,[10b,20] are probably highly involved in this process. The mechanical flexibility of the μ-oxo-linked oligomeric chains evidenced through Raman spectroscopy might also be crucial to the O^{I-} mobility.

In summary, the link observed between the amount of available O^{I-} species and OER performance for the MW compounds indicates that the CO-titration methodology enables a quantitative estimation of OER-relevant O^{I-} species. However, the comparison with AA-IrO_x highlights the need to use additional descriptors for predictions of OER performance, such as the capacity of the samples to exchange surface and subsurface O^{I-} species. The structure-directing effect of the K^+ cations present in the MW iridium oxohydroxides (Table S1) and absent from AA-IrO_x is suggested to be a possible factor that influences the mobility of the O^{I-} species within the microcrystalline environment of the iridium (III/IV) oxohydroxides. An analogy can be seen with the OER-relevant effect of structure-influencing cations in MnO_x electrocatalysts reported recently by Gao et al.[24] In a scenario in which reactive lattice O is involved in the Ir-catalyzed OER, as suggested by Fierro et al.,[19] efficient exchange mechanisms of O^{I-} species play an essential role in the OER reactivity and explain the superior performances of the MW-produced compounds compared with that of AA-IrO_x. This also suggests a three-dimensional aspect of OER catalysis with iridium oxohydroxides, in which subsurface O^{I-} species take part in the catalytic OER.

Low-temperature CO adsorption

Diffuse reflectance infrared spectroscopy (DRIFTS) was used to study the adsorbate structures and intermediates involved in the oxidation of CO on iridium(III/IV) oxohydroxides. However, the quasimetallic properties of iridium oxides constitute a major challenge to the use of IR spectroscopy. For example, IrO_2 was described as a reflector for radiation below its plasma frequency located in the near-IR region.[25] As a result, the reflectance of iridium oxides increases strongly for smaller wavenumbers and inhibits the detection of diffusely scattered light. Conversely, the samples absorb strongly at higher frequencies; therefore, nonlinear backgrounds and noisy spectra are obtained. Hence, only a few studies of the IR spectra of IrO_2 or quasi-amorphous iridium oxide films have been reported.[26]

The present DRIFTS study was performed with the Cl-free MW_5. After the physisorbed water was removed, the sample was characterized mostly by broad IR bands in the $\tilde{\nu}=3700$–$2800\ cm^{-1}$ region (see Figure S10). Broad contributions in the $\tilde{\nu}=3700$–$3450\ cm^{-1}$ region are attributed to isolated OH groups, and contributions in the $\tilde{\nu}=3450$–$3000\ cm^{-1}$ region can be identified as the stretching frequencies of H-bonded OH groups. The great variety of hydroxy groups is in line with the iridium oxohydroxide nature of the samples, which was confirmed by the high hydroxy fraction detected through thermogravimetric analysis.[13] The calculated $Ir^{III/IV}$ trimers (Figures 4 and 5) also showed that hydroxy groups appear in place of the μ-oxo-bridging species as a result of the reduction of Ir^{IV} to Ir^{III}, and this supports the appearance of bulk hydroxy groups in the nanocrystalline iridium oxohydroxide environment.

The contributions observed at $\tilde{\nu}=3000$–$2800\ cm^{-1}$ were attributed by other authors to H-bonded hydroxy groups.[26a] However, this is unlikely at such low wavenumbers, and one should instead consider contamination with C from the atmosphere. Owing to their highly hydrous and hydroxylated surfaces, the iridium oxohydroxides are probably prone to the adsorption of atmospheric contaminants. However, no changes to these spectral contributions were observed during the experiment (Figure S12a); thus, the effect of these C contaminants was assumed to be negligible and irrelevant to CO_2 evolution.

The stepwise adsorption of CO on MW_5 was attempted at liquid-nitrogen temperature to inhibit reactive mechanisms. During the stepwise addition to $P_{eq,CO}=10$ mbar, only minor changes could be observed in the DRIFTS spectra in the $\tilde{\nu}=2000$–$2150\ cm^{-1}$ region in which the CO vibration is expected (Figure S11). The absence of a strong signal indicates that no stable Ir–CO complex was formed at low temperature. Weak adsorption and broad peaks are to be expected as Ir is in an $Ir^{III/IV}$ state, which limits backbonding into the CO π^* orbitals. In keeping with this, CO adsorption studies have mostly been performed with metallic Ir samples[27] or isolated Ir^{III} sites.[28] The adsorption of CO on Ir^{III} is thought to be unstable and was only reported through a reactive process to form iridium(I) carbonyl complexes at higher temperatures.[28a] As a result and in line with our findings, no significant IR signals corresponding to CO adsorbates on iridium(III/IV) oxohydroxides are to be expected between liquid-nitrogen temperature and RT.

After low-temperature CO addition, MW_5 was allowed to warm gradually to RT. The enlarged areas of the spectra recorded during the temperature increase show the appearance of a sharp feature at $\tilde{\nu}=2340\ cm^{-1}$ at approximately $-30\,^{\circ}C$ (Figure S12b). Such a signal corresponds to adsorbed CO_2 produced through the reaction shown in Equation (2). The asymmetric stretching mode of gas-phase CO_2 only shows up at higher temperatures as a broad feature centered at $\tilde{\nu}=2350\ cm^{-1}$. Additional sharper features in the $\tilde{\nu}=2380$–$2320\ cm^{-1}$ range probably correspond to other CO_2 adsorption configurations. The remarkably low onset of CO oxidation at $-30\,^{\circ}C$ confirms the low activation barriers highlighted by Pfei-

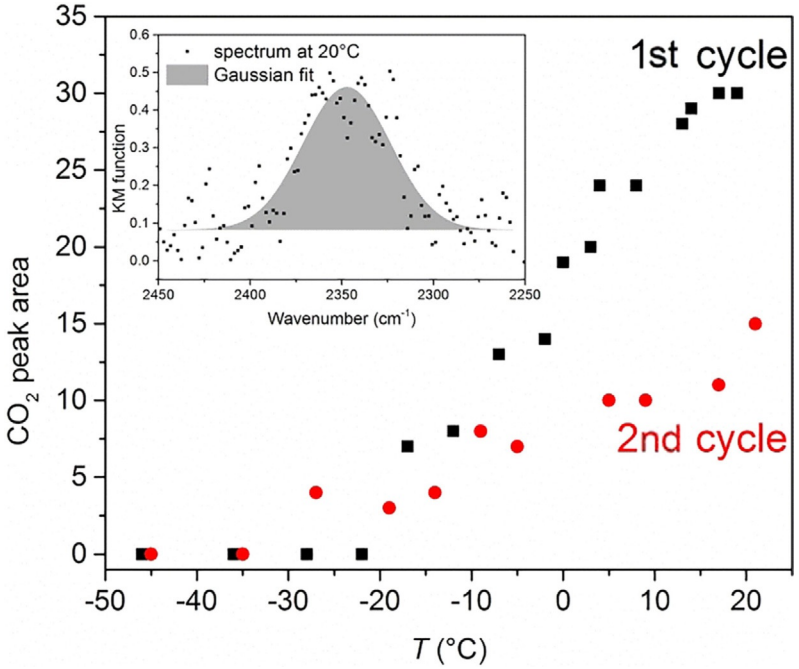

Figure 9. The CO_2-related peak appearing after CO adsorption on MW_5 during the warming procedure from liquid-nitrogen temperature to RT was fitted and integrated with a Gaussian fit model (shown for the spectra obtained at 20 °C in the inset). The determined CO_2 peak areas are reported as a function of *T* for the first (black squares) and second temperature increases (red dots).

fer et al. for reaction with O^{I-} species hosted by iridium(III/IV) oxides.[12] During the temperature increase, a general increase in the intensity of the broad OH feature centered at $\tilde{\nu}=$ 3250 cm^{-1} was also observed (Figure 9a). We suggest that, in conjunction with thermal effects, water present in the bulk samples migrates slowly to the surface with increasing temperature and forms more H bonds.

After the sample was degassed overnight, the CO adsorption at RT was repeated. To compare the first and second temperature increases, the areas under the CO_2-associated peaks were fitted tentatively with a simple Gaussian fit (inset in Figure 9). The integrated peak areas were plotted as a function of temperature (Figure 9), and the plot shows that the second CO addition cycle also resulted in CO_2 evolution at the same onset temperature of approximately −30 °C but with much lower intensity. The low CO pressure used could mean that all of O^{I-} species were not consumed during the first cycle; nonetheless, the discrepancy between CO_2 peak areas confirms the irreversibility of the reaction [Equation (2)]. The early onset for CO oxidation on MW_5 at −30 °C confirms the high electrophilicity of the O^{I-} species hosted by iridium(III/IV) oxohydroxides, in line with the reactivity outlined by Pfeifer et al.[12]

Raman spectra before and after the CO titration

To study the effect of the CO treatment on the structures of the iridium oxohydroxides and possibly identify another spectroscopic signature of the O^{I-} species, MW_5 was placed inside an air-tight cell designed for in situ Raman spectroscopy studies that could be connected to the CO reactor described earlier. The Raman spectra of MW_5 recorded before and after the CO treatment (see Figure S14) showed no significant changes to the broad features attributed to the oxo-bridged iridium(III/IV) oxohydroxide structure. This indicates that the majority of the μ-oxo-bridging species that produce the Raman signals are not consumed during the CO oxidation [Equation (2)]. Even though the theoretical model predicts that the O^{I-} species in Ir^{III}-rich compounds result in μ-bridging O^{I-} species,[10] this only means that these species do not appear as Raman-active modes in the spectrum of iridium(III/IV) oxohydroxides. Nonetheless, the understanding of the Raman spectra of these compounds remains an important point, as O^{I-} species only seem to be hosted within the particular matrix of iridium oxohydroxides.

OER relevance of CO-titrated O^{I-} species

The suggested OER relevance of the electrophilic O^{I-} species[10a,12] prompted us to assess the OER performance of MW_5 before and after the consumption of these species through CO treatment. As shown in Figure 10, the CO titration of the O^{I-} species had a dramatic effect on the OER performance. In terms of OER activity (Figure 10a), the CO treatment resulted in a loss of approximately 59% of $j_\eta = 0.35$ V. The stability during CP at 10 mA cm^{-2} also decreased significantly after the CO treatment, as significantly higher potentials had to be reached at an earlier stage to maintain the anodic current. This clear effect of the CO treatment on the OER performance confirms that the O^{I-} species titrated in the CO experiment play a prominent role in the OER performances of iridium oxohydroxides. More precisely, such electrophilic species

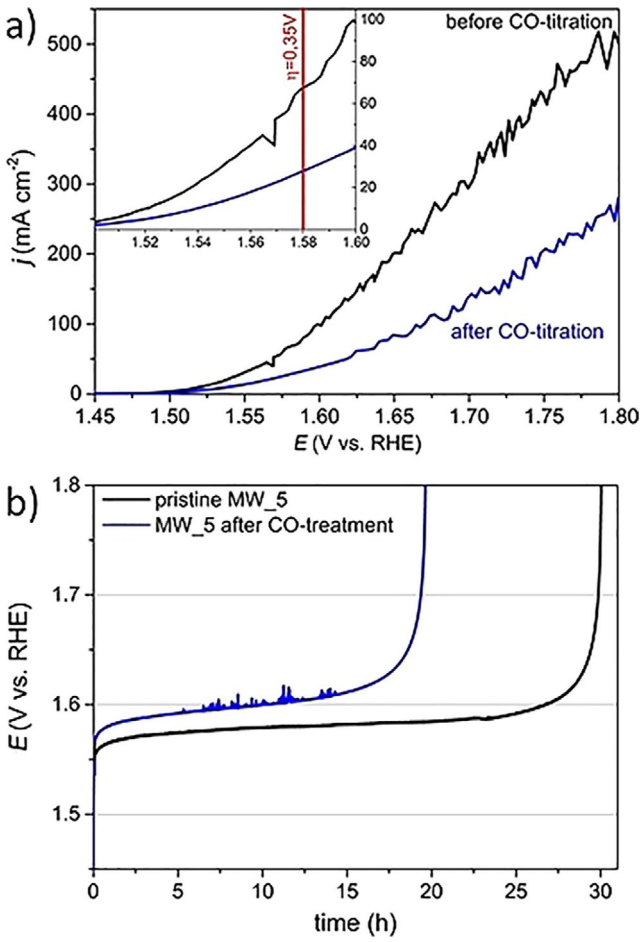

Figure 10. CO-treated MW_5 and pristine MW_5 were tested (a) for OER activity through LSV and (b) for OER stability through CP for electrode loadings of 20 $\mu g_{Ir}\,cm^{-2}$.

are suggested to be involved in the structures of the active-site precursors.

The fact that MW_5 still exhibits relatively high OER reactivity indicates that some performance could be maintained or restored under OER potential despite the strong impact of the CO titration of O^{I-} species. One explanation is that fresh O^{I-} species were exposed during the anode coating process, which involves sonication. However, one should also bear in mind that driving an electrocatalyst to OER potentials also constitutes a preparative activation procedure. It seems likely that OER-relevant species, such as the evidenced O^{I-} species, are regenerated at such potentials. This is in line with the previous observations that the effective preparation of AIROFs requires Ir films to be driven to OER-onset potentials.[3a,b] The authors reported the formation of quasi-amorphous iridium oxohydroxides, which could potentially accommodate O^{I-} species. In such a scenario, as the coated MW_5 is driven to OER potentials after CO treatment, some of the titrated O^{I-} species could reform, and this would explaining the observed residual OER performance. However, the CO titration led to irreversible damage to some of the active sites, and this suggests that O^{I-} species were not the only species consumed. More surface-sensitive methods such as surface-enhanced Raman spectroscopy (SERS) might give access to additional changes caused by the CO titration and help with the identification of other crucial structural features of the active-site precursors.

Conclusions

The careful TEM analysis of the structure of microwave-produced (MW-produced) iridium(III/IV) oxohydroxides confirmed that the nanocrystalline iridium(III/IV) oxohydroxide phase is distinct from rutile IrO_2. The Raman spectroscopy signature of iridium(III/IV) oxohydroxides could be modeled with trimeric Ir structures linked by μ-oxo bridges. Unlike in the rigid rutile lattice of IrO_2, the Ir atoms in such a flexible oligomeric structure can move away from or closer to the O atoms. We suggest that such mechanical flexibility could facilitate oxidation state changes in iridium(III/IV) oxohydroxides during the oxygen evolution reaction (OER).

The μ-oxo-bridging motifs can also be seen as molecular equivalents to the Ir vacancies in the model used by Pfeifer et al. for the electronic structure of iridium(III/IV) oxides.[10a] The suggested presence of OER-relevant reactive O^{I-} species in such iridium(III/IV) oxides[10,12] prompted us to investigate thoroughly the electronic structure of the MW-produced iridium oxohydroxides. X-ray photoemission spectroscopy (XPS) confirmed their mixed $Ir^{III/IV}$ oxidation state. Most importantly, characteristic near-edge X-ray absorption fine structure (NEXAFS) resonance features at the O K-edge at 529 eV revealed the presence of formally O^{I-} species. CO titrations demonstrated the electrophilic character of these O^{I-} species, which reacted with CO even below RT to form CO_2 [Equation (2)]. The resulting CO_2 evolution for the MW-produced iridium(III/IV) oxohydroxides further showed that higher amounts of evolved CO_2 correlated with stronger NEXAFS O^{I-} features and higher OER performance.

Moreover, the results highlighted major differences in the availability and initial reactivity of the O^{I-} species depending on the initial synthesis conditions. Such differences are suggested to be linked to the mobility of the O^{I-} species between the surface and the subsurface of the compounds. Thus, our results highlight the importance of a complementary CO-probe methodology that reveals the availability and reactivity of O^{I-} species detected in iridium(III/IV) oxohydroxides through X-ray absorption spectroscopy (XAS). This is especially the case for comparisons of samples synthesized by different means, for example, the MW-produced compounds and the AA-IrO_x benchmark.

The observations on the electronic structure of the oxygen in the iridium(III/IV) oxohydroxides led us to conclude that electrophilic O^{I-} species stabilized in a highly hydrated, Ir^{III}-rich environment are probably involved in the structures of the precursor sites for the OER catalysis, as suggested by Pfeifer et al.[10a,12] Such electrophilic O species have also been described in the context of the biological OER in Photosystem II.[11] It was suggested that the formation of the O–O bond during the OER could be facilitated through the nucleophilic attack of preadsorbed water or hydroxy groups at the electro-

philic O species accommodated by the Mn-based water oxidation complex [WOC; Eq. (3)].

$$WOC{-}O + H_2O \rightarrow WOC{-}O{-}O{-}H + H^+ + e^- \quad (3)$$

The easy change of oxidation state of the Mn centers in the WOC was found to be key to the preparation of such electrophilic O species. Such an OER scenario, with the electrophilic O species prepared at a mixed-oxidation-state catalytic complex, can be extrapolated to the iridium(III/IV) oxohydroxide electrocatalysts,[10a,12] in line with the OER-involvement of lattice O atoms in Ir electrocatalysts reported by Fierro et al. on the basis of ^{18}O-labelling experiments.[19] These results contrast with the more often reported data that support the "electrochemical oxide" pathway,[29,30] for which the OER mechanism is suggested to involve lattice O species instead of only surface-adsorbed intermediates.

On the basis of the electrophilic reactivity of the O^{I-} species in iridium(III/IV) oxohydroxides and the observed correlation with the OER performance, we confirm the OER relevance of electrophilic O^{I-} species. As suggested by Pfeifer et al.,[12] we propose that these species facilitate O–O bond formation during the OER through the nucleophilic attack of water or preadsorbed hydroxy groups by O^{I-}, and the bottom arrow of the cycle in Figure 11 represents the regeneration of the reactive O^{I-} species under the OER potential. Our CO-titration methodology allowed us to complete this picture by highlighting the possible involvement of subsurface O^{I-} species that can migrate to the surface. Hence, we suggest that a complete OER catalysis model should involve the three-dimensional structure of the iridium(III/IV) oxohydroxides. We propose that high O^{I-} mobility within the iridium(III/IV) oxohydroxide matrix facilitates active-site regeneration under the OER potential. Indeed, after the evolution of O_2, electrophilic O^{I-} species need to be regenerated under anodic potential. Otherwise, if the O^{I-} pool was simply depleted stoichiometrically, our MW-produced iridium oxohydroxides would not be able to maintain stable OER performance.

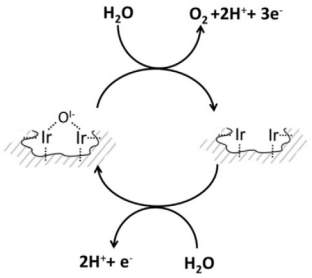

Figure 11. Our results suggest an OER scheme involving O–O bond formation through the nucleophilic attack of the catalytic O^{I-} species in the iridium(III/IV) oxohydroxides under the OER potential.

In general, as several studies have highlighted the formation of quasi-amorphous iridium oxohydroxide-type structures[3a,6a,8a] under OER conditions, we suggest that the active states of Ir-based OER catalysts involve the formation of O^{I-}-containing structures similar to those in our iridium(III/IV) oxohydroxides. Our MW-based synthesis constitutes a particularly efficient strategy, as the synthesized compound is already close in nature to the electrochemically activated state. The result is a compound that accommodates high amounts of precursor sites with a high mobility of reactive O^{I-} species that aids the facile regeneration of the active sites under the OER potential. It remains to be clarified how the immediate environment of the electrophilic O^{I-} species influences their reactivity and mobility.

In conclusion, the synthesis of high-performance iridium(III/IV) oxohydroxide electrocatalysts and the identification of OER-relevant electrophilic O^{I-} species that are mobile within a flexible $Ir^{III/IV}$ matrix constitute significant steps towards a better understanding of this little-studied class of extremely promising OER electrocatalysts. The highlighted results will allow for a more targeted approach towards the preparation of efficient Ir-based OER electrocatalysts for the eventual aim of economically feasible chemical-energy storage through acidic water splitting.

Experimental Section

Sample preparation: The Ir compounds were prepared through the MW-assisted hydrothermal treatment of aqueous precursor solutions containing dissolved potassium hexachloroiridate(IV) (K_2IrCl_6, Alfa Aesar, minimum 39% Ir) and KOH in predefined KOH/Ir ratios. Seven samples were prepared from precursor solutions with initial KOH/Ir ratios ranging from 1:1 to 100:1 for a constant initial Ir concentration of 10^{-2} mol L^{-1}. Four precursor solutions (each 62 mL) were heated in four polytetrafluoroethylene-lined (PTFE-lined) vessels under continuous stirring with a ramp of 10 K min^{-1} and maintained at 250 °C and approximately 55 bar for 60 min in a MW-supported hydrothermal synthesis reactor system (Anton Paar, Multiwave PRO). The vessels were then cooled to RT, and the resulting black Ir compounds were collected by centrifugation at 8000 rpm for 10 min, resuspended in milli-Q water [AppliChem, 18 MΩ, total organic carbon (TOC) < 3 ppb], sonicated for 5 min, and collected again by centrifugation until the conductivity of the supernatant was below 0.05 mS cm^{-1}. The powders were subsequently dried at 80 °C for 12 h and ground in a mortar. The compositions, specific surface areas (S_{BET}), and average Ir oxidation states listed in Table S1 were determined by the methods described elsewhere.[13]

Transmission electron microscopy: We used an aberration-corrected TITAN 80-300 instrument operated at 80 kV. The dry powder samples were dispersed in water, and the dispersions were ultrasonicated for 5 min. The dispersions were drop-cast between two graphene/quantifoil grids, left to dry, and inserted into the microscope.

Photoemission and absorption measurements: The measurements were performed at the ISISS beamline at BESSYII/HZB (Berlin, Germany).[31] The powders were pressed into self-supporting wafers (40 mg, 3 t, Ø = 8 mm) and subsequently measured in ultrahigh vacuum (UHV; $\approx 10^{-6}$ Pa). The binding-energy calibration was performed after an evaluation of each corresponding Fermi edge. For the NEXAFS measurements, the photon energy was scaled continuously between 525 and 560 eV by moving the monochromator. The total electron yield (TEY) of the O K-edge was collected with a Faraday cup with an applied accelerating voltage.

The XPS spectra were fitted after the subtraction of a Shirley background with the commercially available CasaXPS software (www.casaxps.com). In all fits, the peak separations and peak-area ratios between the $Ir4f_{7/2}$ and the $Ir4f_{5/2}$ components were constrained to 3 eV and 4:3, respectively. Deviations in the peak-area ratios of 5% were allowed to account for the inaccuracies in the background subtraction and peak-area determination of asymmetric peaks. The employed fit parameters for rutile IrO_2 and the quasi-amorphous iridium(III/IV) oxide are listed elsewhere.[10]

Raman spectroscopy: The Raman spectroscopy was performed at 532 nm excitation wavelength with a confocal microscope setup (S&I GmbH, Warstein, Germany) equipped with a PyLoN:2kBUV CCD camera and a 750 mm focal-length monochromator (Princeton Instruments). The laser-intensity density on the samples was chosen to be low enough to preclude the decomposition of the iridium oxohydroxide structure. At higher laser intensities, the appearance of sharp peaks corresponding to rutile modes indicated the transformation of the iridium oxohydroxide into rutile IrO_2 owing to local heating. The spectra were averaged over multiple measurements at different spots of the sample.

DFT calculations of the Ir structures and Raman spectra: All calculations were performed with the ORCA package.[32] Structural models of monomeric $Ir(OH)_6^{2-}$ and dimeric $(OH)_2(H_2O)_2Ir(\mu\text{-}O^{2-})_2Ir(OH)_2(H_2O)_2$ up to pentameric units were constructed by hand, and their geometries were subsequently optimized [B3LYP functional,[33] Def2-TZVP basis set,[34] relativistic corrections by zeroth order regular approximation (ZORA),[35] dispersion corrections according to Grimme et al.].[36] The calculations of the Raman spectra were performed by the method implemented in ORCA. The Cartesian coordinates of each model are provided as Supporting Information.

Reference samples: We compared our results to those for two Ir reference compounds previously used in our study on the electronic structure of iridium oxide:[10a] a nanocrystalline iridium oxohydroxide close in nature to our samples (Premion, Alfa Aesar, denoted AA-IrO_x) and a crystalline rutile-type IrO_2 (Sigma–Aldrich, denoted SA-IrO_2).

Electrochemical tests: The electrode loadings were 20 $\mu g_{Ir}\,cm^{-2}$ in all cases. The OER activity was assessed through linear sweep voltammetry (LSV) at a sweep rate of 5 $mV\,s^{-1}$ from the open-circuit potential (E_{oc}) to 1.8 V versus the reversible hydrogen electrode (RHE). The mass-specific current obtained at 350 mV overpotential was used as an activity indicator for comparison. The stabilities were assessed through CP experiments at 15 (accelerated testing conditions) and 10 $mA\,cm^{-2}$. The samples were considered deactivated if the working-electrode potential (E_{WE}) reached 1.8 V versus RHE to avoid oxidative damage to the glassy carbon (GC) electrode support. The corresponding graphs are reported elsewhere.[10b,13]

Room-temperature CO oxidation: The CO oxidation at RT was used as a stoichiometric titration reaction of the reactive O species. The Ir samples [25 mg of the catalyst, diluted by 250 mg of inert SiC (particle diameter: 250–355 μm)] were exposed to a 1% CO/He flow (100 $mL\,min^{-1}$). The samples were dried in He at RT for 1 h before the experiments. The switch from inert He to a 1% CO/He stream (both 100 $mL\,min^{-1}$) was performed with a six-port switching valve (Valco, Vici) that excluded dead volumes. For the reactivation test of fresh MW_5 after the first CO treatment, the He was saturated with water through a gas-tight H_2O bubbler connected to the He line through a bypass.

DRIFTS of low-temperature CO adsorption: The DRIFTS spectra were recorded with a mercury cadmium telluride (MCT) detector at a resolution of 4 cm^{-1}; 1024 scans were accumulated with a Praying MantisTM reaction chamber (ZnSe window) placed in a Bruker IFS 66 spectrometer controlled by the OPUS software. The in situ cell was equipped with a liquid-nitrogen cooling system and connected to a vacuum pump. A background spectrum of pure KBr was recorded at RT. MW_5 was degassed under vacuum at 40 °C overnight before the measurements. After the samples cooled to 77 K, CO (Westfalen, >99.99% purity) was added stepwise until a pressure of 10 mbar was reached. The sample was then left to warm gradually to RT and left in CO overnight. After evacuation under vacuum, this cycle was repeated a second time.

Abbreviations

AIROF, anodically grown iridium oxide film; HRTEM, high-resolution transmission electron microscopy; LSV, linear sweep voltammetry; MW, microwave; NAP, near-ambient pressure; NEXAFS, near-edge X-ray absorption fine structure; OER, oxygen evolution reaction; ROS, reactive oxygen species; RT, room temperature; S_{BET}, BET-derived specific surface area; TPR, temperature-programmed reduction; WOC, water oxidation complex; XAS, X-ray absorption spectroscopy; XPS, X-ray photoemission spectroscopy; $\chi_{H_2O,chem}$, mass fraction of chemisorbed water.

Acknowledgements

Financial support came from the German Federal Ministry for Economic Affairs and Energy (BMWi) in the framework of the "Ekolyser" project (no. 03ESP106D). We thank the HZB for the allocation of beamtime at the Bessy II synchrotron radiation source. Our special thanks go to Detre Teschner and Andrey Tarasov for their thorough proofreading of the present work and fruitful scientific discussions.

Conflict of interest

The authors declare no conflict of interest.

Keywords: electrochemistry · energy storage · iridium · oxygen · water splitting

[1] a) C. C. L. McCrory, S. Jung, I. M. Ferrer, S. M. Chatman, J. C. Peters, T. F. Jaramillo, *J. Am. Chem. Soc.* **2015**, *137*, 4347; b) I. Katsounaros, S. Cherevko, A. R. Zeradjanin, K. J. J. Mayrhofer, *Angew. Chem. Int. Ed.* **2014**, *53*, 102; *Angew. Chem.* **2014**, *126*, 104; c) M. Bernicke, E. Ortel, T. Reier, A. Bergmann, J. Ferreira de Araujo, P. Strasser, R. Kraehnert, *ChemSusChem* **2015**, *8*, 1908.

[2] J. O. M. Bockris, T. Otagawa, *J. Electrochem. Soc.* **1984**, *131*, 290.

[3] a) E. J. Frazer, R. Woods, *J. Electroanal. Chem. Interfacial Electrochem.* **1979**, *102*, 127; b) M. Vuković, *J. Appl. Electrochem.* **1987**, *17*, 737; c) T. Reier, M. Oezaslan, P. Strasser, *ACS Catal.* **2012**, *2*, 1765.

[4] G. Beni, L. M. Schiavone, J. L. Shay, W. C. Dautremont-Smith, B. S. Schneider, *Nature* **1979**, *282*, 281.

[5] a) S. Cherevko, T. Reier, A. R. Zeradjanin, Z. Pawolek, P. Strasser, K. J. J. Mayrhofer, *Electrochem. Commun.* **2014**, *48*, 81; b) T. Reier, D. Teschner, T. Lunkenbein, A. Bergmann, S. Selve, R. Kraehnert, R. Schlögl, P. Strasser, *J. Electrochem. Soc.* **2014**, *161*, F876.

[6] a) U. Hintermair, S. W. Sheehan, A. R. Parent, D. H. Ess, D. T. Richens, P. H. Vaccaro, G. W. Brudvig, R. H. Crabtree, *J. Am. Chem. Soc.* **2013**, *135*, 10837; b) O. Diaz-Morales, T. J. P. Hersbach, D. G. H. Hetterscheid, J. N. H. Reek, M. T. M. Koper, *J. Am. Chem. Soc.* **2014**, *136*, 10432; c) J. Huang, J. D. Blakemore, D. Fazi, O. Kokhan, N. D. Schley, R. H. Crabtree, G. W. Brudvig, D. M. Tiede, *Phys. Chem. Chem. Phys.* **2014**, *16*, 1814.

[7] Y. Zhao, N. M. Vargas-Barbosa, M. E. Strayer, N. S. McCool, M.-E. Pandelia, T. P. Saunders, J. R. Swierk, J. F. Callejas, L. Jensen, T. E. Mallouk, *J. Am. Chem. Soc.* **2015**, *137*, 8749.

[8] a) A. Minguzzi, C. Locatelli, O. Lugaresi, E. Achilli, G. Cappelletti, M. Scavini, M. Coduri, P. Masala, B. Sacchi, A. Vertova, P. Ghigna, S. Rondinini, *ACS Catal.* **2015**, *5*, 5104; b) A. Minguzzi, O. Lugaresi, E. Achilli, C. Locatelli, A. Vertova, P. Ghigna, S. Rondinini, *Chem. Sci.* **2014**, *5*, 3591.

[9] H. G. Sanchez Casalongue, M. L. Ng, S. Kaya, D. Friebel, H. Ogasawara, A. Nilsson, *Angew. Chem. Int. Ed.* **2014**, *53*, 7169; *Angew. Chem.* **2014**, *126*, 7297.

[10] a) V. Pfeifer, T. E. Jones, J. J. Velasco Vélez, C. Massué, R. Arrigo, D. Teschner, F. Girgsdies, M. Scherzer, M. T. Greiner, J. Allan, M. Hashagen, G. Weinberg, S. Piccinin, M. Hävecker, A. Knop-Gericke, R. Schlögl, *Surf. Interface Anal.* **2016**, *48*, 261; b) V. Pfeifer, T. E. Jones, J. J. Velasco Vélez, C. Massué, M. T. Greiner, R. Arrigo, D. Teschner, F. Girgsdies, M. Scherzer, J. Allan, M. Hashagen, G. Weinberg, S. Piccinin, M. Hävecker, A. Knop-Gericke, R. Schlögl, *Phys. Chem. Chem. Phys.* **2016**, *18*, 2292.

[11] W. Lubitz, E. J. Reijerse, J. Messinger, *Energy Environ. Sci.* **2008**, *1*, 15.

[12] V. Pfeifer, T. E. Jones, S. Wrabetz, C. Massue, J. J. Velasco Velez, R. Arrigo, M. Scherzer, S. Piccinin, M. Havecker, A. Knop-Gericke, R. Schlögl, *Chem. Sci.* **2016**, *7*, 6791.

[13] C. Massué, X. Huang, A. Tarasov, C. Ranjan, S. Cap, R. Schlögl, *ChemSusChem* **2017**, *10*, 1958.

[14] Y.-Z. Wang, Y.-X. Zhao, C.-G. Gao, D.-S. Liu, *Catal. Lett.* **2008**, *125*, 134.

[15] a) G. Algara-Siller, S. Kurasch, M. Sedighi, O. Lehtinen, U. Kaiser, *Appl. Phys. Lett.* **2013**, *103*, 203107; b) R. Zan, Q. M. Ramasse, R. Jalil, T. Georgiou, U. Bangert, K. S. Novoselov, *ACS Nano* **2013**, *7*, 10167.

[16] C. Gammer, C. Mangler, C. Rentenberger, H. P. Karnthaler, *Scr. Mater.* **2010**, *63*, 312.

[17] Y. S. Huang, S. S. Lin, C. R. Huang, M. C. Lee, T. E. Dann, F. Z. Chien, *Solid State Commun.* **1989**, *70*, 517.

[18] J. F. Moulder, J. Chastain, R. C. King, *Handbook of X-ray Photoelectron Spectroscopy: A Reference Book of Standard Spectra for Identification and Interpretation of XPS Data*, PerkinElmer, Eden Prairie, MN, **1992**.

[19] S. Fierro, T. Nagel, H. Baltruschat, C. Comninellis, *Electrochem. Commun.* **2007**, *9*, 1969.

[20] T. Reier, Z. Pawolek, S. Cherevko, M. Bruns, T. Jones, D. Teschner, S. Selve, A. Bergmann, H. N. Nong, R. Schlögl, K. J. J. Mayrhofer, P. Strasser, *J. Am. Chem. Soc.* **2015**, *137*, 13031.

[21] P. Kast, M. Friedrich, D. Teschner, F. Girgsdies, T. Lunkenbein, R. Naumann d'Alnoncourt, M. Behrens, R. Schlögl, *Appl. Catal. A* **2015**, *502*, 8.

[22] M. G. Willinger, W. Zhang, O. Bondarchuk, S. Shaikhutdinov, H.-J. Freund, R. Schlögl, *Angew. Chem. Int. Ed.* **2014**, *53*, 5998; *Angew. Chem.* **2014**, *126*, 6108.

[23] J. Lin, B. Qiao, L. Li, H. Guan, C. Ruan, A. Wang, W. Zhang, X. Wang, T. Zhang, *J. Catal.* **2014**, *319*, 142.

[24] Q. Gao, C. Ranjan, Z. Pavlovic, R. Blume, R. Schlögl, *ACS Catal.* **2015**, *5*, 7265.

[25] S. H. Brewer, D. Wicaksana, J.-P. Maria, A. I. Kingon, S. Franzen, *Chem. Phys.* **2005**, *313*, 25.

[26] a) S. Ito, Y. Abe, M. Kawamura, K. H. Kim, *J. Vac. Sci. Technol. B* **2015**, *33*, 041204; b) R. O. Lezna, K. Kunimatsu, T. Ohtsuka, N. Sato, *J. Electrochem. Soc.* **1987**, *134*, 3090.

[27] a) T. S. Marinova, D. V. Chakarov, *Surf. Sci.* **1989**, *217*, 65; b) D. Reinalda, V. Ponec, *Surf. Sci.* **1980**, *91*, 113; c) S. Zou, R. Gómez, M. J. Weaver, *Langmuir* **1997**, *13*, 6713.

[28] a) P. Gelin, G. Coudurier, Y. B. Taarit, C. Naccache, *J. Catal.* **1981**, *70*, 32; b) M. Mihaylov, E. Ivanova, F. Thibault-Starzyk, M. Daturi, L. Dimitrov, K. Hadjiivanov, *J. Phys. Chem. B* **2006**, *110*, 10383.

[29] R. Kötz, H. Neff, S. Stucki, *J. Electrochem. Soc.* **1984**, *131*, 72.

[30] D. Finkelstein-Shapiro, M. Fournier, D. D. Méndez-Hernández, C. Guo, M. Calatayud, T. A. Moore, A. L. Moore, D. Gust, J. L. Yarger, *Phys. Chem. Chem. Phys.* **2017**, *19*, 16151 – 16158.

[31] A. Knop-Gericke, E. Kleimenov, M. Hävecker, R. Blume, D. Teschner, S. Zafeiratos, R. Schlögl, V. I. Bukhtiyarov, V. V. Kaichev, I. P. Prosvirin, A. I. Nizovskii, H. Bluhm, A. Barinov, P. Dudin, M. Kiskinova in *Advanced Catalysis, Vol. 52*, Elsevier, Amsterdam **2009**, pp. 213 – 272.

[32] F. Neese, *Wiley Interdiscip. Rev.: Comput. Mol. Sci.* **2012**, *2*, 73.

[33] A. D. Becke, *Phys. Rev. A* **1988**, *38*, 3098.

[34] D. A. Pantazis, X.-Y. Chen, C. R. Landis, F. Neese, *J. Chem. Theory Comput.* **2008**, *4*, 908.

[35] E. van Lenthe, J. G. Snijders, E. J. Baerends, *J. Chem. Phys.* **1996**, *105*, 6505.

[36] S. Grimme, S. Ehrlich, L. Goerigk, *J. Comput. Chem.* **2011**, *32*, 1456.

Manuscript received: July 17, 2017
Revised manuscript received: August 29, 2017
Accepted manuscript online: September 21, 2017
Version of record online: November 8, 2017

